APPLIED PHYSICS

Origin of unusual bandgap shift and dual emission in organic-inorganic lead halide perovskites

M. Ibrahim Dar,[1]*† Gwénolé Jacopin,[2†] Simone Meloni,[3‡] Alessandro Mattoni,[4] Neha Arora,[1] Ariadni Boziki,[3] Shaik Mohammed Zakeeruddin,[1] Ursula Rothlisberger,[3] Michael Grätzel[1]

Emission characteristics of metal halide perovskites play a key role in the current widespread investigations into their potential uses in optoelectronics and photonics. However, a fundamental understanding of the molecular origin of the unusual blueshift of the bandgap and dual emission in perovskites is still lacking. In this direction, we investigated the extraordinary photoluminescence behavior of three representatives of this important class of photonic materials, that is, $CH_3NH_3PbI_3$, $CH_3NH_3PbBr_3$, and $CH(NH_2)_2PbBr_3$, which emerged from our thorough studies of the effects of temperature on their bandgap and emission decay dynamics using time-integrated and time-resolved photoluminescence spectroscopy. The low-temperature (<100 K) photoluminescence of $CH_3NH_3PbI_3$ and $CH_3NH_3PbBr_3$ reveals two distinct emission peaks, whereas that of $CH(NH_2)_2PbBr_3$ shows a single emission peak. Furthermore, irrespective of perovskite composition, the bandgap exhibits an unusual blueshift by raising the temperature from 15 to 300 K. Density functional theory and classical molecular dynamics simulations allow for assigning the additional photoluminescence peak to the presence of molecularly disordered orthorhombic domains and also rationalize that the unusual blueshift of the bandgap with increasing temperature is due to the stabilization of the valence band maximum. Our findings provide new insights into the salient emission properties of perovskite materials, which define their performance in solar cells and light-emitting devices.

INTRODUCTION

Advancement in the performance of organic-inorganic metal halide perovskite solar cells and light-emitting devices has been remarkable over the last few years; however, an understanding of the fundamental properties of these perovskite materials is still evolving (*1*). In a light-harnessing or light-emitting device, bandgap, absorption coefficient, and excitonic properties of the light absorber or emitter play critical roles in determining its performance (*2*, *3*). Arguably, the perovskite materials exhibit all the desired properties that make them potential candidates for the fields of photovoltaics, light-emitting devices, field effect transistors, and lasers (*4*–*7*). Bandgap modulation, spontaneous dissociation of excitons, and long-range balanced electron- and hole-diffusion lengths in the perovskite materials are among the main distinctive properties that have led to an unprecedented evolution of efficient perovskite solar cells (*8*, *9*).

To gain deeper insight into the photophysical processes occurring in the perovskite materials (*10*–*14*), it is worth exploring them at low temperatures where the additional complexity induced by thermal effects is minimized. Although in the literature different perovskite materials have been studied using various kinds of spectroscopies, there have been only a few exhaustive reports regarding temperature-dependent photoluminescence (PL) studies (*15*, *16*). Investigating the temperature-dependent optoelectronic properties of hybrid organic-inorganic perovskites could be of interest for the identification of their potential for particular technological applications, such as space power applications. Therefore, exploring emission characteristics of a perovskite absorber across a wide temperature range, particularly at low temperatures, can provide important clues regarding the performance of a light-emitting device and solar cell based on perovskites (*17*). Previous studies reported the temperature dependence of PL and an additional emission peak in $CH_3NH_3PbI_3$ at low temperature (*7*, *18*–*20*). However, a fundamental understanding of the molecular origin of the unusual blueshift of the bandgap and dual emission in perovskites is still evolving (*21*–*23*).

Here, we systematically explored the temperature dependence of the bandgap and decay kinetics of emission in $CH_3NH_3PbI_3$, $CH_3NH_3PbBr_3$, and $CH(NH_2)_2PbBr_3$ using time-integrated and time-resolved PL spectroscopy. The low-temperature (<100 K) time-integrated PL studies of $CH_3NH_3PbI_3$ and $CH_3NH_3PbBr_3$ highlighted the presence of a well-defined second emission peak, whereas $CH(NH_2)_2PbBr_3$ exhibited a single emission peak. The emission dynamics demonstrated the transfer of charge carriers from the high-energy emission peak to the low-energy emission peak. In addition to the lack of comprehensive experimental results regarding temperature-dependent PL studies of perovskites, there is no unequivocal theoretical interpretation of the existing data. To bridge this gap, we have carried out density functional theory (DFT) calculations and classical molecular dynamics (MD) simulations to identify the molecular origin of the experimentally observed temperature- and composition-dependent emission characteristics of perovskites. Our in-depth investigation provides new fundamental insights into the emission characteristics of this important class of photonic materials—the lead halide perovskites.

RESULTS

Organic-inorganic metal halide perovskites exhibit the general formula ABX_3 (where A is a monovalent organic cation, B is Pb^{2+} or Sn^{2+}, and X is a halide anion) (*24*). To obtain $CH_3NH_3PbI_3$, $CH_3NH_3PbBr_3$, and $CH(NH_2)_2PbBr_3$ films, we used solution-based

[1]Laboratory of Photonics and Interfaces, Institute of Chemical Sciences and Engineering, École Polytechnique Fédérale de Lausanne, CH-1015 Lausanne, Switzerland. [2]Laboratory of Quantum Optoelectronics, Institute of Physics, École Polytechnique Fédérale de Lausanne, CH-1015 Lausanne, Switzerland. [3]Laboratory of Computational Chemistry and Biochemistry, Institute of Chemical Sciences and Engineering, École Polytechnique Fédérale de Lausanne, CH-1015 Lausanne, Switzerland. [4]Istituto Officina dei Materiali, CNR-IOM SLACS Cagliari, Cittadella Universitaria, Monserrato (CA) 09042-I, Italy.
*Corresponding author. Email: ibrahim.dar@epfl.ch
†These authors contributed equally to this work.
‡Present address: Department of Mechanical and Aerospace Engineering, Sapienza University of Rome, via Eudossiana 18, 00184 Rome, Italy.

deposition methods (see Materials and Methods) (*25*, *26*). X-ray diffraction (XRD) (fig. S1) and field emission scanning electron microscopy (fig. S2) established the formation of phase-pure and homogeneous perovskite films, respectively (*27*).

Emission characteristics of $CH_3NH_3PbI_3$

The structural characterization based on XRD (fig. S1) confirmed the formation of the tetragonal phase of $CH_3NH_3PbI_3$, which is thermodynamically the most stable phase at room temperature (*28*). Below 160 K, the tetragonal phase transforms into an orthorhombic phase, whereas above 330 K, $CH_3NH_3PbI_3$ stabilizes into a cubic phase (*29*, *30*). Furthermore, using time-integrated and time-resolved PL spectroscopy, we have explored in detail the temperature dependence of the bandgap and the dynamics of emission in $CH_3NH_3PbI_3$ perovskite films deposited on mesoporous Al_2O_3.

Temperature-dependent PL

Exploring the PL of hybrid organic-inorganic perovskites over a wide range of temperature is not only of fundamental interest but also aims to identify the practical applications of the devices based on these perovskites. Figure 1A shows the time-integrated PL of the $CH_3NH_3PbI_3$ film recorded at 15 K, which highlights the presence of two emission peaks located at 1.574 and 1.649 eV (Fig. 1B). While increasing the temperature to 80 K, the low-energy emission peak experienced a blueshift of 15 meV (from 1.574 to 1.589 eV). Likewise, the central energy of the high-energy emission peak attributable to the orthorhombic phase of $CH_3NH_3PbI_3$ exhibits a blueshift of 25 meV (from 1.649 to 1.674 eV) before disappearing above 120 K (Fig. 1B). This widening of the bandgap is in apparent discord with the usual Varshni behavior of standard tetrahedral semiconductors in which the bandgap experiences a redshift with the increase in temperature (*31*). Furthermore, while raising the temperature from 15 to 75 K, the linewidth or full width at half maximum (FWHM) of the low-energy emission peak unusually decreases by 7 meV (from 77 to 70 meV), whereas the FWHM of the high-energy emission peak increases from 39 to 43 meV (Fig. 1C). At 75 K, the low-energy emission peak commences to redshift from 1.589 to 1.569 eV up to 150 K, which is also followed by a decrease in the linewidth from 70 to 56 meV (Fig. 1B). From 150 to 300 K, the single emission peak attributed to the tetragonal phase reveals a systematic blueshift of 32 meV (from 1.569 eV at 150 K to 1.601 eV at 300 K) (Fig. 1B), with concurrent enhancement in the linewidth from 56 to 87 meV (Fig. 1C).

The evolution of the FWHM of emission peaks that correspond to the orthorhombic and tetragonal phases (Fig. 1C) can be fitted by taking into account the temperature-independent inhomogeneous broadening (Γ_0) and the interaction between charge carriers and LO-phonons, described by the Fröhlich Hamiltonian (*32*, *33*). The extracted fitting values [Γ_0 = 39 meV; charge carrier LO-phonon coupling strength (γ_{LO}) = 40 meV; and energy of LO-phonon (E_{LO}) = 15 meV] agree with the literature (Fig. 1C) (*33*). The intensity of emission peaks corresponding to the orthorhombic (high-energy peak below 120 K) and tetragonal phases (above 150 K) (Fig. 1D) continuously

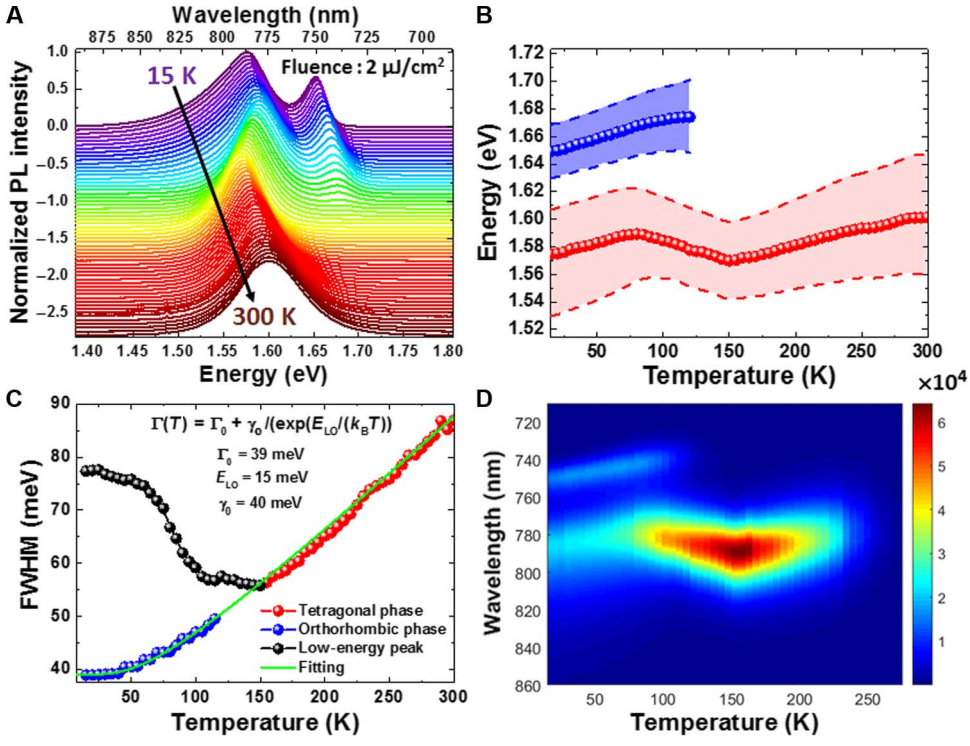

Fig. 1. Temperature-dependent emission characteristics of $CH_3NH_3PbI_3$ (fluence = 2 μJ/cm²). (**A**) Normalized PL intensity of $CH_3NH_3PbI_3$ as a function of temperature recorded from 15 to 300 K (spectra have been vertically shifted for clarity). (**B**) Position of the PL peaks corresponding to the low energy and the orthorhombic and tetragonal phases of $CH_3NH_3PbI_3$ as a function of temperature. (**C**) FWHM of the PL peaks corresponding to the low energy and the orthorhombic and tetragonal phases of $CH_3NH_3PbI_3$ as a function of temperature. Green solid line shows the fitting obtained by taking into account the temperature-independent inhomogeneous broadening (Γ_0) and the interaction between charge carriers and longitudinal optical phonons (LO-phonons), as described by the Fröhlich Hamiltonian. (**D**) Absolute intensity of PL spectra corresponding to the low-energy emission peak and the orthorhombic and tetragonal phases of $CH_3NH_3PbI_3$ as a function of temperature from 15 to 300 K.

diminishes with increasing temperature, which could arguably be attributed to the activation of nonradiative recombination centers. The PL intensity is maximal around 150 K (Fig. 1D), which implies that $CH_3NH_3PbI_3$ could be a strong emitter around 140 to 160 K (*7*). The intensity and linewidth of the low-energy emission peak (Fig. 1D) do not follow the trend exhibited by the orthorhombic (high-energy peak below 120 K) and tetragonal (above 150 K) phases. The emission from the low-energy peak increases considerably from 75 to 150 K.

Fluence-dependent PL

It is well known that the accumulation of charges during photoexcitation increases the inherent bandgap of the $CH_3NH_3PbI_3$ (*34*). Therefore, to further understand the dependence of the position and intensity of the three PL peaks on the excitation energy densities, we investigated the emission characteristics of $CH_3NH_3PbI_3$ at 15 and 300 K using different laser fluences (Fig. 2). With increasing fluence, a continuous blueshift of the low-energy emission peak from 1.436 eV at 0.1 nJ/cm^2 up to 1.536 eV at 4.5 μJ/cm^2 was observed at 15 K (Fig. 2, A and B), which could be attributed to the band filling effect (*34*). On the other hand, the high-energy emission peak exhibits a blueshift only at higher fluences (>0.2 μJ/cm^2). This suggests that the charge transfer from the orthorhombic phase of $CH_3NH_3PbI_3$ to the low-energy emission peak occurs at lower fluences (<0.2 μJ/cm^2), whereas at higher fluences (>0.2 μJ/cm^2) the band filling effect predominates over a dynamic charge transfer. At 300 K, no noticeable shift in the position of the single PL peak assigned to the tetragonal phase of $CH_3NH_3PbI_3$ was observed over a range of excitation intensities (Fig. 2, D and E). Figure 2 (C and F) displays the dependence of PL intensity on the fluence recorded at 15 and 300 K. At 15 K, we observe a perfectly linear relationship between the fluence (<0.2 μJ/cm^2) and the integrated PL intensity over more than five orders of magnitude for both the high-energy and low-energy emission peaks, which confirms the absence of nonradiative recombination at low temperature. In contrast, at 300 K, the integrated PL intensity of the tetragonal phase of $CH_3NH_3PbI_3$ shows an overlinear dependence on the fluence. At higher fluences, an enhancement in the carrier density leads to the saturation of nonradiative recombination centers, which improves the effective internal quantum efficiency. No signature of reduction in effective internal quantum efficiency was observed for the tetragonal phase of $CH_3NH_3PbI_3$, which suggests that Auger recombination plays a minimal role under this fluence.

Temperature- and fluence-dependent time-resolved PL

From the fluence-dependent emission studies of $CH_3NH_3PbI_3$, we observed the transfer of charge carriers from the high-energy (orthorhombic phase) to the low-energy emission peak at 15 K. To further unravel the charge transfer process and to understand the effect of temperature and fluence on charge carrier dynamics in $CH_3NH_3PbI_3$, we explored time-resolved PL.

With increasing fluence, the charge carrier lifetime (τ_{10}, time at which the maximum PL intensity reduces by a factor of 10) continuously decreases in the low-energy emission peak (15 K) (Fig. 3, A and B) as well as in the tetragonal phase (300 K) of $CH_3NH_3PbI_3$ (Fig. 3, E and F). For a given fluence at 15 K, the charge carriers are relatively long-lasting in the low-energy emission peak (Fig. 3A), as compared to those in the high-energy emission peak (orthorhombic phase) (Fig. 3C).

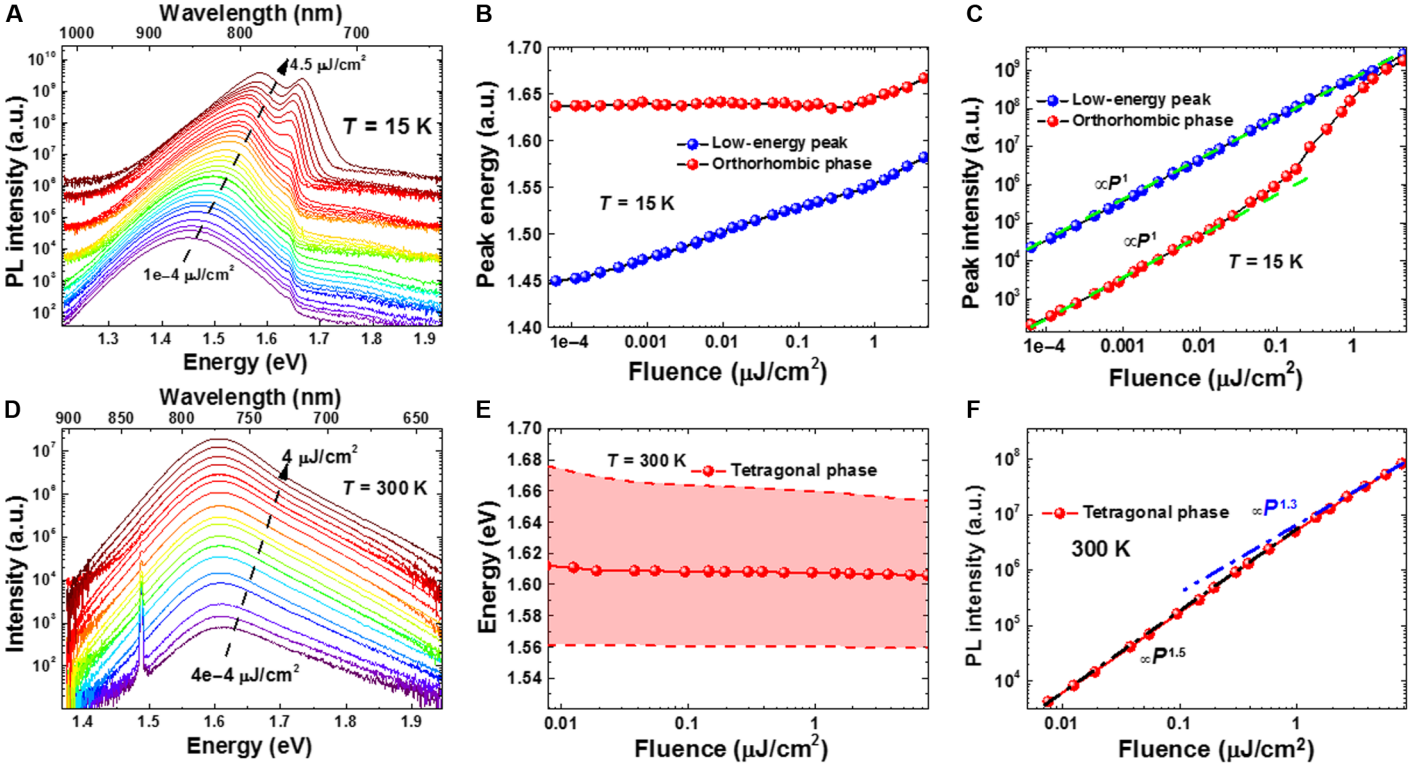

Fig. 2. Fluence-dependent emission characteristics of $CH_3NH_3PbI_3$ recorded at 15 and 300 K. (**A**) PL spectra of the low- and high-energy emission peaks as a function of fluence recorded at 15 K. (**B**) Position of the low- and high-energy emission peaks as a function of fluence recorded at 15 K. (**C**) Intensity of the low- and high-energy emission peaks as a function of fluence recorded at 15 K. (**D**) PL spectra of the tetragonal phase as a function of fluence recorded at 300 K. (**E**) Position of the tetragonal emission peak as a function of fluence recorded at 300 K. (**F**) Intensity of the tetragonal emission peak as a function of fluence recorded at 300 K.

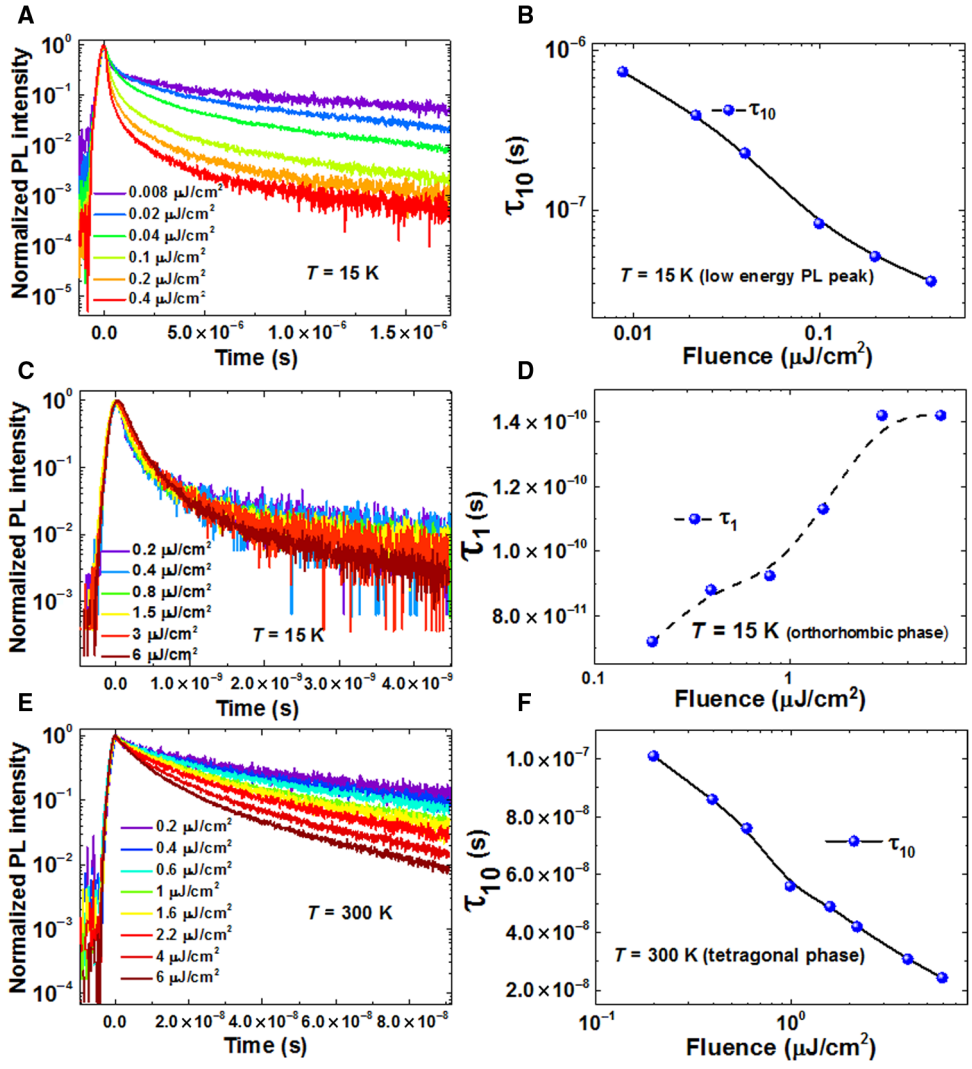

Fig. 3. Time-resolved PL of $CH_3NH_3PbI_3$ performed at 15 and 300 K. (**A**) Fluence-dependent time-resolved PL of the low-energy emission peak recorded at 15 K. (**B**) Charge carrier lifetime (τ_{10}) in the low-energy emission peak decreases with increasing fluence recorded at 15 K. (**C**) Fluence-dependent time-resolved PL of the high-energy emission peak (orthorhombic phase) recorded at 15 K. (**D**) Charge carrier lifetime (τ_1, faster component) in the high-energy emission peak (orthorhombic phase) increases with increasing fluence recorded at 15 K. (**E**) Fluence-dependent time-resolved PL of the tetragonal phase recorded at 300 K. (**F**) Charge carrier lifetime (τ_{10}) decreases with increasing fluence in the tetragonal phase recorded at 300 K. (τ_{10}, time at which the maximum PL intensity decreases by a factor of 10).

The recombination dynamics in the orthorhombic phase at 15 K unusually relaxes (Fig. 3, C and D) within a nanosecond range at higher fluences, which implies that relaxation occurs through processes other than pure charge carrier recombination. We envisage that this strange behavior of carrier dynamics involves the charge transfer from the orthorhombic phase into the low-energy emission peak, in addition to the recombination of the carriers (see Discussion). When carrier lifetime exceeds ~0.5 ns, the decay dynamics shows a normal trend, that is, the higher the fluence, the faster the recombination dynamics.

At 300 K, the lifetime (τ_{10}) decreases with increasing fluence in the tetragonal phase, which can be explained by evoking the bimolecular recombination mechanism (the charges predominantly exist as free carriers) (Fig. 3, E and F). However, because of the concurrent nonradiative recombination of charge carriers, the bimolecular recombination rate and fluence do not follow the linear trend, which agrees with the overlinear dependence of PL intensity on fluence, observed at 300 K (Fig. 2F). Overall, the charge carrier lifetime increases while raising the temperature from 15 to 300 K (fig. S6), which indicates that the charge carrier dynamics involves bimolecular recombination.

Temperature-dependent emission characteristics of $CH_3NH_3PbBr_3$

The thorough analysis of emission characteristics established that $CH_3NH_3PbI_3$ exhibits a dual emission at low temperature and widening of the bandgap with the increase in temperature. To substantiate these unusual spectral features, we examined $CH_3NH_3PbBr_3$, another representative of the organic-inorganic lead halide perovskite family. $CH_3NH_3PbBr_3$ crystallizes in the cubic phase at room temperature (fig. S1) (*35*). By replacing the iodide with bromide, the bandgap increases from 1.61 eV in $CH_3NH_3PbI_3$ to 2.36 eV in $CH_3NH_3PbBr_3$ at 300 K (*36*). The PL spectrum of $CH_3NH_3PbBr_3$ also displays two emission peaks located at 2.28 and 2.36 eV at 15 K (Fig. 4A), which

confirms that the origin of dual emission is not associated with the nature of the halide ion in methylammonium (MA; $CH_3NH_3^+$)–based perovskites. The nature of the halide ion has negligible impact on the difference in the positions of two emission peaks, which is ~75 to 80 meV for both $CH_3NH_3PbI_3$ and $CH_3NH_3PbBr_3$. Below 175 K, the FWHM of the high-energy emission peak does not show any temperature dependence and remains constant around 65 meV (Fig. 4B). On the contrary, the linewidth of the low-energy emission peak increases from 40 meV at 75 K to 130 meV at 300 K. With increased temperature, the high-energy emission peak showed a maximal shift of 45 meV before disappearing above 175 K, whereas the low-energy emission peak revealed a continuous blueshift of 74 meV (from 2.285 eV at 15 K to 2.359 eV at 300 K) up to 300 K (Fig. 4C).

Temperature-dependent emission characteristics of $CH(NH_2)_2PbBr_3$

Thus far, we observed that the presence of the additional emission peak remains unaffected when replacing iodide with bromide in MA-based perovskites. To get further insight into the origin of dual emission at low temperature, we replaced MA with a formamidinium [FA; $CH(NH_2)_2^+$] cation in bromide-based perovskite. Surprisingly, this replacement led to the disappearance of the distinct second emission peak (Fig. 4D), which implies that the origin of the dual emission is associated with the nature of the organic cation (*37*). As compared to $CH_3NH_3PbBr_3$ perovskite, the $CH(NH_2)_2PbBr_3$ sample exhibits a narrower linewidth at both low and high temperatures (Fig. 4E), which indicates that peak broadening is also associated with the nature of organic cations. Furthermore, the energy of the single emission peak increases with temperature from 2.20 eV at 25 K to 2.22 eV at 150 K, and between 150 and 175 K, the position of the PL peak shifts by 9 meV (Fig. 4F), which could possibly be attributed to a phase transition. The emission peak exhibited a continuous blueshift of 54 meV when the temperature was raised to 300 K.

Theoretical study

To identify the origin of peculiar emission characteristics, such as the widening of the bandgap and the dependence of dual emission on the nature of the organic cation, we performed classical MD on large systems (~25,000 atoms) in combination with DFT calculations. Previously, it has been established that in the tetragonal phase of $CH_3NH_3PbI_3$ (T > 160 K; Fig. 5), MA cations reorient on a picosecond time scale, resulting in a dynamical molecular disorder (*29*, *30*, *38*–*40*), whereas in the orthorhombic phase of $CH_3NH_3PbI_3$, MA cations tend to align because of the constraints imposed by the PbI_3 framework (fig. S9) (*38*–*40*). However, classical MD simulations show that upon the cooling of a large tetragonal structure below the transition temperature, it is possible to kinetically trap MA in disordered configurations, leading to the formation of MA-disordered domains in an otherwise ordered orthorhombic phase of $CH_3NH_3PbI_3$ (Fig. 5A) (*41*). It is worth emphasizing that the disordered domains are not

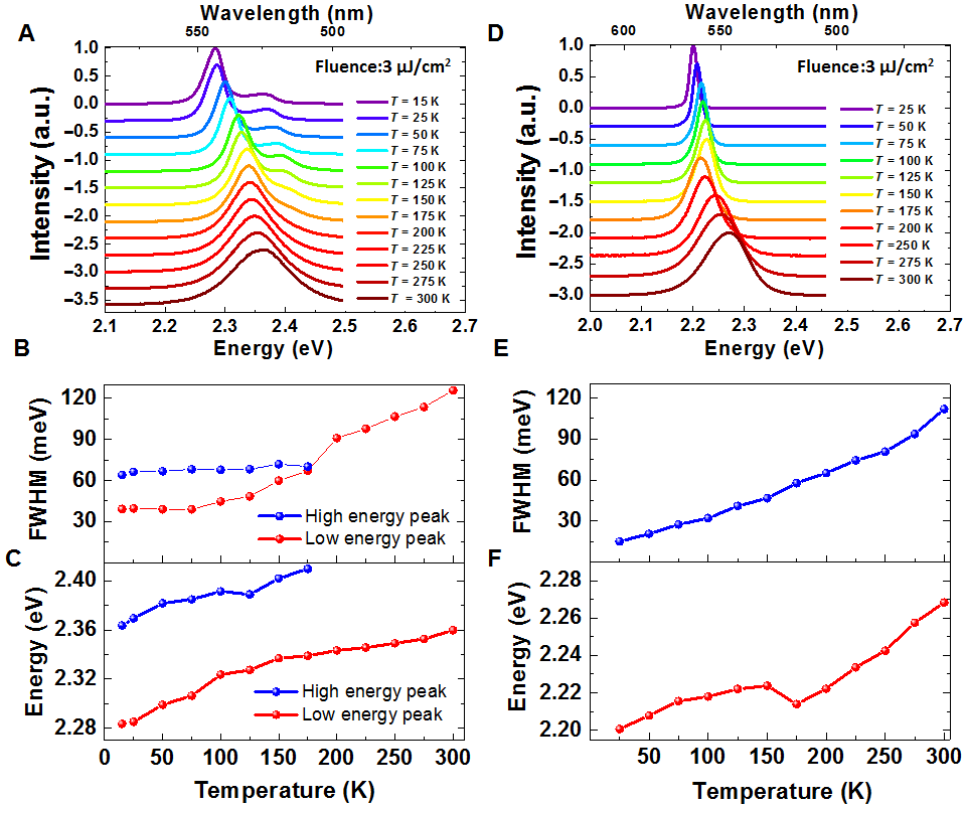

Fig. 4. Temperature-dependent emission characteristics of $CH_3NH_3PbBr_3$ (A to C) and $CH(NH_2)_2PbBr_3$ (D to F) perovskite (fluence = 3 μJ/cm²). (**A**) Normalized PL intensity of $CH_3NH_3PbBr_3$ as a function of temperature. (**B**) FWHM of the low- and high-energy emission peaks of $CH_3NH_3PbBr_3$ as a function of temperature. (**C**) Position of the low- and high-energy emission peaks of $CH_3NH_3PbBr_3$ as a function of temperature. (**D**) Normalized PL intensity of $CH(NH_2)_2PbBr_3$ as a function of temperature. (**E**) FWHM of the PL peak of $CH(NH_2)_2PbBr_3$ as a function of temperature. (**F**) Position of the PL peak of $CH(NH_2)_2PbBr_3$ as a function of temperature. [Note that because of better structural stability, $CH(NH_2)_2PbBr_3$ was chosen over $CH(NH_2)_2PbI_3$.]

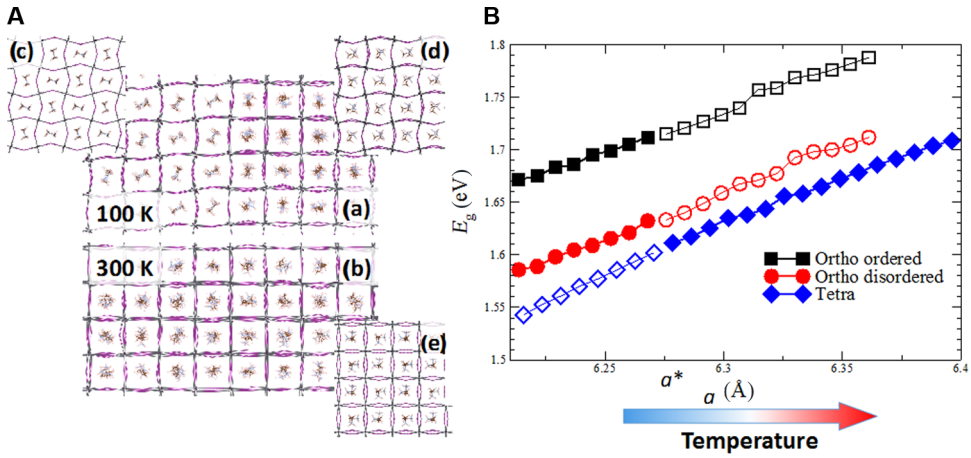

Fig. 5. Classical MD simulations. (**A**) Snapshots extracted from the classical MD simulations at (a) 100 K and (b) 300 K. Panels (c), (d), and (e) show the configurations of the samples used in the first-principles electronic structure calculations of the MA-ordered and MA-disordered orthorhombic and the tetragonal systems, respectively. Periodic boundary conditions are applied to improve the visualization. (**B**) E_g as a function of the pseudocubic lattice parameter, $a = \sqrt[3]{V}$ (V, volume per stoichiometric unit) for the MA-ordered (black symbols) and MA-disordered (red symbols) orthorhombic systems and the tetragonal system (blue symbols). E_g of the orthorhombic systems is computed starting from the computational equilibrium lattice. Subsequently, the lattice is isotropically expanded over a range of ~0.2 Å. The E_g of the tetragonal phase is computed over the same range as a. Open and filled symbols are introduced to improve readability, highlighting the change in the E_g across the phase transition. For the orthorhombic systems, filled symbols refer to a lattice parameter over a range of ~0.05 Å, consistent with the literature (*29*). Filled symbols for the tetragonal system are used in the complementary range.

tetragonal inclusions but rather orthorhombic domains with a molecular disorder, which is further confirmed by comparing the Pb-I partial pair correlation function, $g^{PbI}(r)$, of the disordered and ordered orthorhombic domains with the tetragonal phase (fig. S10A) and the existing literature (*41*). DFT band structure calculations show (Fig. 5B) that the MA-ordered domains [Fig. 5A (a)] have an ~85 meV larger bandgap (E_g) than the MA-disordered ones [Fig. 5A (d)], in agreement with the experimental results recorded at low temperature (Fig. 1). This supports the hypothesis that the two PL peaks are associated with MA-ordered and MA-disordered domains in $CH_3NH_3PbI_3$. In the ordered domains, the alignment of MA cations produces a strong local electric field, which eventually increases the E_g of MA-ordered orthorhombic domains (Stark-like effect) (*42*). Furthermore, after MA cations were removed (and Pb^{2+} and I^- were kept fixed at their original positions), the computational study reveals the reduction of the ΔE_g between ordered and disordered domains by ~65 meV, establishing the fact that MA alignment majorly splits the peaks (~85 meV) with the Stark-like effect.

To investigate the origin of the effect of temperature on the PL peak position, we computed the E_g of the various systems as a function of the pseudocubic lattice parameter, $a = \sqrt[3]{V}$. Figure 5B shows that E_g grows with a, suggesting that the blueshift of the PL peaks with temperature is due to the thermal expansion of the $CH_3NH_3PbI_3$ lattice. Consequently, this expansion reduces the overlap between Pb-6s and I-5p antibonding atomic orbitals, forming the valence band maximum (VBM; fig. S11), which increases the overall bandgap of $CH_3NH_3PbI_3$ (*43*, *44*). Between 120 and 150 K, that is, below the orthorhombic to tetragonal phase transition temperature of $CH_3NH_3PbI_3$ (<160 K), the experiments show two phenomena: (i) the high-energy PL peak disappears, and (ii) the low-energy peak smoothly shifts toward lower energies. Fundamentally, the disappearance of the high-energy emission peak is associated with the rotational mobility of the MA cations in the tetragonal phase of $CH_3NH_3PbI_3$ (*38*–*40*, *42*, *45*). Concerning the evolution of the low-energy emission peak, the mobility of MA cations in disordered orthorhombic domains gradually increases with temperature and eventually leads to a smooth transition into a regular tetragonal phase. This is further illustrated by a smooth change of the second set of peaks in the $g^{PbI}(r)$ of the disordered domains in temperatures ranging from 100 to 150 K (fig. S10C), which reduces E_g by ~20 meV (Fig. 5B), in excellent agreement with the redshift observed experimentally (Figs. 1A and 4A).

DISCUSSION

The existence of a dual emission peak at low temperature in $CH_3NH_3PbI_3$ perovskite agrees with previous studies; however, its origin has remained inconclusive so far (*18*). Xing *et al.* (*7*) assigned three emission peaks to two bound-exciton emissions (815 and 782 nm) and a free-exciton emission (higher energy), whereas Kong *et al.* (*19*) attributed them to a donor-acceptor pair (low energy) and free-exciton transitions. Fang *et al.* (*20*) ascribed the low- and high-energy emission peaks to free and bound excitons, respectively. Wehrenfennig *et al.* (*46*) and Panzer *et al.* (*47*) concluded the presence of tetragonal inclusions in the orthorhombic phase at low temperature (*46*, *47*). These hypotheses have not been confirmed theoretically and are insufficient to explain the complete phenomenology presented in this work (Figs. 1 to 4). For example, tetragonal inclusions are not possible in $CH_3NH_3PbBr_3$, which exists in the cubic phase at room temperature and thus cannot explain why the well-distinct additional emission peak disappears in the $CH(NH_2)_2PbBr_3$ perovskite. Here, we propose a theoretical model supported by simulation results, which can explain all the observed trends of the PL spectra over the entire temperature range (15 to 300 K) for all perovskite systems.

Our calculations suggest that the difference in E_g between the ordered and disordered domains arises from the relatively higher energy of VBM in the latter domains (fig. S12). Therefore, the migration of photogenerated carriers from the ordered domains to the disordered ones becomes energetically feasible (Fig. 2A). At low fluence, the charge carriers from the wide bandgap (ordered) domains are transferred to the low bandgap (disordered) domains (fig. S13A),

and the recombination of charge carriers predominantly occurs in the latter domains (black spectrum, fig. S13D). Because of the absorption of more photons at intermediate fluences and the transfer of carriers from the ordered domains (high-energy emission peak) to the disordered domains (low-energy emission peak) (fig. S13B), the accumulation of the charges shifts the emission peak toward higher energy (band filling effect) (red spectrum, fig. S13D). At fluences greater than 0.2 $\mu J/cm^2$, the band filling effect predominates over the charge transfer process (fig. S13C); thus, both the emission peaks corresponding to the ordered and disordered orthorhombic domains become prominent (green spectrum, fig. S13D).

Replacing iodide with bromide does not induce any significant qualitative difference, that is, ordered and disordered domains with a ΔE_g of ~85 meV still exit through the Stark-like effect, corroborating the experimental results (~80 meV) (Fig. 4). However, when MA is replaced with a less polar monovalent cation [for example, FA (fig. S14), which exhibits a smaller dipole moment (μ_{FA} = 0.2 D versus μ_{MA} = 2.3 D) (*48*)], the intensity of the Stark-like effect diminishes, and the calculated peak splitting in the $CH(NH_2)_2PbBr_3$ (~10 to 20 meV) becomes smaller than the linewidth. Even if ordered and disordered domains form in $CH(NH_2)_2PbBr_3$ perovskite, it will be difficult to resolve their emission features under these conditions.

The unconventional temperature effects on the intensity and linewidth of the emission peak ascribed to the disordered orthorhombic domains of $CH_3NH_3PbI_3$ demand more attention because possible insights could further help in unfolding the promising emission characteristics of perovskites. The unusual broadening observed at low temperature could be explained by evoking the thermally activated microstructure evolution of the material and the dynamics of MA cations within the inorganic framework. The MD reveals that the disordered phase is composed of zones with different degrees of local alignment of MA cations. Eventually, different local molecular dipoles result in slightly different energies, which translate into a broad emission peak. Above 50 K, the temperature progressively activates the evolution of microstructure with molecular rearrangements and reduces the disordered phase (and thus the linewidth), whereas the energy of the low-energy emission peak tends to reach the energy of the tetragonal phase.

In conclusion, we demonstrated the temperature dependence of decay dynamics of emissions in $CH_3NH_3PbI_3$, $CH_3NH_3PbBr_3$, and $CH(NH_2)_2PbBr_3$. We have rationally addressed the unusual blueshift of the bandgap with temperature and the dual emission at low temperature (<100 K). With the help of MD and first-principles calculations, the blueshift in the bandgap could be attributed to the stabilization of the VBM, and the presence of the well-defined two emission peaks revealed by MA-based perovskites at low temperature is caused by the coexistence of MA-ordered and MA-disordered orthorhombic domains. $CH(NH_2)_2PbBr_3$ exhibits only a single emission feature at low temperature because the difference between ordered and disordered domains is much smaller [~10 to 20 meV in $CH(NH_2)_2PbBr_3$ versus ~80 to 90 meV in MA-perovskites] than the linewidth. Overall, our in-depth study presents intriguing results into the temperature-dependent emission properties and bandgap modulation of lead halide perovskites.

MATERIALS AND METHODS

Materials

All materials were purchased from Sigma-Aldrich and used as received unless stated otherwise.

Photoanode preparation

A 250-nm-thick Al_2O_3 mesoporous layer was deposited on a precleaned nonconducting glass substrate. Before the deposition of the Al_2O_3 mesoporous layer, the glass substrate was cleaned with a detergent, rinsed with deionized water and ethanol, and then treated in an ultraviolet/O_3 cleaner for 10 min. Subsequently diluted [1:3.5 (w/w) ratio] Al_2O_3 mesoporous paste containing 30 nm of Al_2O_3 nanoparticles (homemade) was spin-coated (5000 rpm, acceleration of 2000 rpm for 30 s) onto the glass substrate. After sintering by following a series of steps (325°C for 5 min with a 15-min ramp time, 375°C for 5 min with a 5-min ramp time, 450°C for 15 min with a 5-min ramp time, and 500°C for 15 min with a 5-min ramp time), mesoporous Al_2O_3 films were obtained.

Preparation of perovskite samples

Synthesis of the $CH_3NH_3PbI_3$ and $CH(NH_2)_2PbBr_3$ samples involved a sequential deposition method with some modifications. One molar solutions of PbI_2 (TCI, 99.99%) and $PbBr_2$ (TCI, 99%) were prepared, respectively, in *N*,*N*′-dimethylformamide (DMF) and DMF-dimethylsulfoxide (DMSO) [1:1 (v/v)] solvent mixture by constant stirring at 100°C for 10 min. Mesoporous Al_2O_3 photoanode films were coated with PbI_2 or $PbBr_2$ by spin-coating the corresponding precursor solutions (1 M) at 6500 rpm for 30 s, and the films were dried at 70°C for 15 min. After the lead halide films were cooled to room temperature, a 200-µl solution of CH_3NH_3I (Dyesol) in 2-propanol (8 mg/ml) was spin-coated on the PbI_2 film with a delay of 120 s for 30 s, whereas the $PbBr_2$ films were dipped into 50 mM solutions of $CH(NH_2)_2I$ (Dyesol) in 2-propanol for 15 min. For the preparation of $CH_3NH_3PbBr_3$, a single-step methodology was used. Typically, 50 µl of a reaction mixture containing 1 mol of each $PbBr_2$ and CH_3NH_3Br (Dyesol) dissolved in 1 ml of DMF-DMSO [1:1 (v/v)] solvent mixture was deposited onto mesoporous photoanode films by spin-coating at 2000 rpm for 30 s. All the resulting perovskite films were annealed at 110°C for 15 min.

Structural and morphological characterization

XRD data acquired from perovskite films were collected on a Bruker Advance D8 x-ray diffractometer with a graphite monochromator, using Cu-K_α radiation, at a scanning rate of 1 deg/min. A field-emission scanning electron microscope (Merlin) was used to examine the surface morphology of the perovskite films. An electron beam accelerated to 3 kV was used with an in-lens detector.

Spectroscopic characterization

Different perovskite samples were analyzed using time-integrated and time-resolved PL spectroscopy as a function of the temperature. All samples were excited from the perovskite side with the second harmonic (~425 nm) of a picosecond mode-locked Ti/sapphire laser (80.5 MHz). The excitation beam was focused on the sample by means of a 90-mm focal that allows for an excitation spot diameter of around 100 µm. The collected PL spectra were spectrally and temporally analyzed using a 32-cm focal length monochromator equipped with a charge-coupled device, which has a spectral resolution of >1 meV and a streak camera with a temporal resolution of ~20 ps.

Computational section

Classical MD simulations were performed by the DL_POLY package (*49*) by using a force field recently developed by Mattoni *et al.* (*39*). We considered computational samples of several sizes, ranging from ~900 to ~25,000 atoms. Periodic boundary conditions were applied along the

three directions. Samples were first equilibrated at 300 K and 1 bar by NPT (constant number of atoms, pressure, and temperature) MD and then quenched and aged at several temperatures (100, 150, 200, and 300 K), still allowing the volume to change according to the temperature and pressure. The smooth transition was investigated by a 10-ns-long classical MD at 10 K intervals ranging from 100 to 150 K.

First-principles calculations were performed within the framework of the generalized gradient approximation to DFT. In particular, we used the Perdew-Burke-Ernzerhof exchange and correlation functional (*50*). The interaction between valence electrons and core electrons and nuclei was described by Rappe-Rabe-Kaxiras-Joannopulos pseudopotentials (*51*). Kohn-Sham orbitals were expanded in a plane wave basis set with a cutoff of 40 Ry (rydberg), and the Brillouin zone was sampled with a shifted $4 \times 4 \times 4$ Monkhorst-Pack k-point grid (*52*). These values were chosen by checking the convergence of total energy, bandgap, and atomic forces. All first-principles calculations were performed using the Quantum Espresso package (*53*). The samples for the first-principles calculations of $CH_3NH_3PbI_3$ were prepared starting from the unit cell classical MD samples. In particular, the orthogonal random sample was obtained starting from the ordered one, and the MA cations were randomly rotated. After geometry and cell optimization, the simulation box was isotropically expanded and compressed over a range of ~1.5% of the pseudocubic lattice parameter, $a = \sqrt[3]{V}$ (V, volume per stoichiometric unit). At each given value of the lattice, the geometry of the system was relaxed, and the E_g was computed on the relaxed structure. $CH_3NH_3PbBr_3$ samples were prepared starting from the corresponding $CH_3NH_3PbI_3$ ones by shrinking the lattice to match the experimental value. Then, the geometries and the cells were optimized, and the E_g values were computed. In the case of $CH(NH_2)_2PbBr_3$, we started from the experimental structure of $CH(NH_2)_2PbI_3$ (*54*), replaced I with Br, and let the geometry and cell relax. The orientation of the FA cations was changed to produce a configuration that is analogous to that of ordered and disordered $CH_3NH_3PbI_3$ and $CH_3NH_3PbBr_3$, with the C–H pointing along the same direction as the C–N bonds. The geometry and cell were then optimized, and the bandgap was calculated for the optimized structure.

SUPPLEMENTARY MATERIALS

Supplementary material for this article is available at http://advances.sciencemag.org/cgi/content/full/2/10/e1601156/DC1

fig. S1. Structural characterization of perovskite films.
fig. S2. Scanning electron microscopy analysis of perovskite films.
fig. S3. Streak camera image of the time-resolved PL measurements recorded from the $CH_3NH_3PbI_3$ film sample at 15 and 300 K.
fig. S4. Streak camera image of the time-resolved PL measurements recorded from the $CH_3NH_3PbBr_3$ film sample at 15 and 300 K.
fig. S5. Streak camera image of the time-resolved PL measurements recorded from the $CH(NH_2)_2PbBr_3$ film sample at 15 and 300 K.
fig. S6. Time-resolved PL of $CH_3NH_3PbI_3$ as a function of temperature (fluence = 2 μJ/cm^2).
fig. S7. Time-resolved PL of $CH_3NH_3PbBr_3$ as a function of temperature (fluence = 3 μJ/cm^2).
fig. S8. Time-resolved PL of $CH(NH_2)_2PbBr_3$ as a function of temperature (fluence = 3 μJ/cm^2).
fig. S9. Structure of the ideal orthorhombic phase.
fig. S10. Pb-I pair correlation function of the MA-ordered and MA-disordered domains of the orthorhombic system and of the tetragonal phase.
fig. S11. VBM of the MA-ordered and MA-disordered orthorhombic systems and of the tetragonal system.
fig. S12. Band structure of the ordered and random domains of the orthorhombic phase of $CH_3NH_3PbI_3$.
fig. S13. Scheme illustrating possible absorption, relaxation, and emission mechanisms at low temperature in $CH_3NH_3PbI_3$ and $CH_3NH_3PbBr_3$.
fig. S14. Configurations of the samples used in the first-principles electronic structure calculations.

REFERENCES AND NOTES

1. M. A. Green, A. Ho-Baillie, H. J. Snaith, The emergence of perovskite solar cells. *Nat. Photonics* **8**, 506–514 (2014).
2. K. Tvingstedt, O. Malinkiewicz, A. Baumann, C. Deibel, H. J. Snaith, V. Dyakonov, H. J. Bolink, Radiative efficiency of lead iodide based perovskite solar cells. *Sci. Rep.* **4**, 6071 (2014).
3. U. Rau, Reciprocity relation between photovoltaic quantum efficiency and electroluminescent emission of solar cells. *Phys. Rev. B* **76**, 085303 (2007).
4. A. Kojima, K. Teshima, Y. Shirai, T. Miyasaka, Organometal halide perovskites as visible-light sensitizers for photovoltaic cells. *J. Am. Chem. Soc.* **131**, 6050–6051 (2009).
5. Z.-K. Tan, R. S. Moghaddam, M. L. Lai, P. Docampo, R. Higler, F. Deschler, M. Price, A. Sadhanala, L. M. Pazos, D. Credgington, F. Hanusch, T. Bein, H. J. Snaith, R. H. Friend, Bright light-emitting diodes based on organometal halide perovskite. *Nat. Nanotechnol.* **9**, 687–692 (2014).
6. C. R. Kagan, D. B. Mitzi, C. D. Dimitrakopoulos, Organic-inorganic hybrid materials as semiconducting channels in thin-film field-effect transistors. *Science* **286**, 945–947 (1999).
7. G. Xing, N. Mathews, S. S. Lim, N. Yantara, X. Liu, D. Sabba, M. Grätzel, S. Mhaisalkar, T. C. Sum, Low-temperature solution-processed wavelength-tunable perovskites for lasing. *Nat. Mater.* **13**, 476–480 (2014).
8. G. Xing, N. Mathews, S. Sun, S. S. Lim, Y. M. Lam, M. Grätzel, S. Mhaisalkar, T. C. Sum, Long-range balanced electron- and hole-transport lengths in organic-inorganic $CH_3NH_3PbI_3$. *Science* **342**, 344–347 (2013).
9. S. D. Stranks, G. E. Eperon, G. Grancini, C. Menelaou, M. J. P. Alcocer, T. Leijtens, L. M. Herz, A. Petrozza, H. J. Snaith, Electron-hole diffusion lengths exceeding 1 micrometer in an organometal trihalide perovskite absorber. *Science* **342**, 341–344 (2013).
10. M. I. Saidaminov, A. L. Abdelhady, B. Murali, E. Alarousu, V. M. Burlakov, W. Peng, I. Dursun, L. Wang, Y. He, G. Maculan, A. Goriely, T. Wu, O. F. Mohammed, O. M. Bakr, High-quality bulk hybrid perovskite single crystals within minutes by inverse temperature crystallization. *Nat. Commun.* **6**, 7586 (2015).
11. K. G. Stamplecoskie, J. S. Manser, P. V. Kamat, Dual nature of the excited state in organic–inorganic lead halide perovskites. *Energy Environ. Sci.* **8**, 208–215 (2015).
12. D. W. de Quilettes, S. M. Vorpahl, S. D. Stranks, H. Nagaoka, G. E. Eperon, M. E. Ziffer, H. J. Snaith, D. S. Ginger, Impact of microstructure on local carrier lifetime in perovskite solar cells. *Science* **348**, 683–686 (2015).
13. C. G. Bischak, E. M. Sanehira, J. T. Precht, J. M. Luther, N. S. Ginsberg, Heterogeneous charge carrier dynamics in organic–inorganic hybrid materials: Nanoscale lateral and depth-dependent variation of recombination rates in methylammonium lead halide perovskite thin films. *Nano Lett.* **15**, 4799–4807 (2015).
14. Y. Yang, D. P. Ostrowski, R. M. France, K. Zhu, J. van de Lagemaat, J. M. Luther, M. C. Beard, Observation of a hot-phonon bottleneck in lead-iodide perovskites. *Nat. Photonics* **10**, 53–59 (2016).
15. N. Sestu, M. Cadelano, V. Sarritzu, F. Chen, D. Marongiu, R. Piras, M. Mainas, F. Quochi, M. Saba, A. Mura, G. Bongiovanni, Absorption F-sum rule for the exciton binding energy in methylammonium lead halide perovskites. *J. Phys. Chem. Lett.* **6**, 4566–4572 (2015).
16. V. D'Innocenzo, G. Grancini, M. J. P. Alcocer, A. R. S. Kandada, S. D. Stranks, M. M. Lee, G. Lanzani, H. J. Snaith, A. Petrozza, Excitons versus free charges in organo-lead tri-halide perovskites. *Nat. Commun.* **5**, 3586 (2014).
17. M. I. Dar, G. Jacopin, M. Hezam, N. Arora, S. M. Zakeeruddin, B. Deveaud, M. K. Nazeeruddin, M. Grätzel, Asymmetric cathodoluminescence emission in $CH_3NH_3PbI_{3-x}Br_x$ perovskite single crystals. *ACS Photonics* **3**, 947–952 (2016).
18. K. Wu, A. Bera, C. Ma, Y. Du, Y. Yang, L. Li, T. Wu, Temperature-dependent excitonic photoluminescence of hybrid organometal halide perovskite films. *Phys. Chem. Chem. Phys.* **16**, 22476–22481 (2014).
19. W. Kong, Z. Ye, Z. Qi, B. Zhang, M. Wang, A. Rahimi-Iman, H. Wu, Characterization of an abnormal photoluminescence behavior upon crystal-phase transition of perovskite $CH_3NH_3PbI_3$. *Phys. Chem. Chem. Phys.* **17**, 16405–16411 (2015).
20. H.-H. Fang, R. Raissa, M. Abdu-Aguye, S. Adjokatse, G. R. Blake, J. Even, M. A. Loi, Photophysics of organic-inorganic hybrid lead iodide perovskite single crystals. *Adv. Funct. Mater.* **25**, 2378–2385 (2015).
21. R. L. Milot, G. E. Eperon, H. J. Snaith, M. B. Johnston, L. M. Herz, Temperature-dependent charge-carrier dynamics in $CH_3NH_3PbI_3$ perovskite thin films. *Adv. Funct. Mater.* **25**, 6218–6227 (2015).
22. Y. Yamada, T. Nakamura, M. Endo, A. Wakamiya, Y. Kanemitsu, Photoelectronic responses in solution-processed perovskite $CH_3NH_3PbI_3$ solar cells studied by photoluminescence and photoabsorption spectroscopy. *IEEE J. Photovolt.* **5**, 401–405 (2015).
23. E. S. Parrott, R. L. Milot, T. Stergiopoulos, H. J. Snaith, M. B. Johnston, L. M. Herz, Effect of structural phase transition on charge-carrier lifetimes and defects in $CH_3NH_3SnI_3$ perovskite. *J. Phys. Chem. Lett.* **7**, 1321–1326 (2016).
24. M. Grätzel, The light and shade of perovskite solar cells. *Nat. Mater.* **13**, 838–842 (2014).
25. J.-H. Im, I.-H. Jang, N. Pellet, M. Grätzel, N.-G. Park, Growth of $CH_3NH_3PbI_3$ cuboids with controlled size for high-efficiency perovskite solar cells. *Nat. Nanotechnol.* **9**, 927–932 (2014).

26. M. I. Dar, N. Arora, P. Gao, S. Ahmad, M. Grätzel, M. K. Nazeeruddin, Investigation regarding the role of chloride in organic–inorganic halide perovskites obtained from chloride containing precursors. *Nano Lett.* **14**, 6991–6996 (2014).
27. N. Onoda-Yamamuro, T. Matsuo, H. Suga, Dielectric study of $CH_3NH_3PbX_3$ (X = Cl, Br, I). *J. Phys. Chem. Solids* **53**, 935–939 (1992).
28. T. Baikie, Y. Fang, J. M. Kadro, M. Schreyer, F. Wei, S. G. Mhaisalkar, M. Graetzel, T. J. White, Synthesis and crystal chemistry of the hybrid perovskite $(CH_3NH_3)PbI_3$ for solid-state sensitised solar cell applications. *J. Mater. Chem. A* **1**, 5628–5641 (2013).
29. A. Poglitsch, D. Weber, Dynamic disorder in methylammoniumtrihalogenoplumbates (II) observed by millimeter-wave spectroscopy. *J. Chem. Phys.* **87**, 6373–6378 (1987).
30. M. T. Weller, O. J. Weber, P. F. Henry, A. M. Di Pumpo, T. C. Hansen, Complete structure and cation orientation in the perovskite photovoltaic methylammonium lead iodide between 100 and 352 K. *Chem. Commun.* **51**, 4180–4183 (2015).
31. Y. P. Varshni, Temperature dependence of the energy gap in semiconductors. *Phys. Chem. Chem. Phys.* **34**, 149–154 (1967).
32. C. Wehrenfennig, M. Liu, H. J. Snaith, M. B. Johnston, L. M. Herz, Homogeneous emission line broadening in the organo lead halide perovskite $CH_3NH_3PbI_{3-x}Cl_x$. *J. Phys. Chem. Lett.* **5**, 1300–1306 (2014).
33. A. D. Wright, C. Verdi, R. L. Milot, G. E. Eperon, M. A. Pérez-Osorio, H. J. Snaith, F. Giustino, M. B. Johnston, L. M. Herz, Electron–phonon coupling in hybrid lead halide perovskites. *Nat. Commun.* **7**, 11755 (2016).
34. J. S. Manser, P. V. Kamat, Band filling with free charge carriers in organometal halide perovskites. *Nat. Photonics* **8**, 737–743 (2014).
35. N. Onoda-Yamamuro, O. Yamamuro, T. Matsuo, H. Suga, *p-T* phase relations of $CH_3NH_3PbX_3$ (X = Cl, Br, I) crystals. *J. Phys. Chem. Solid* **53**, 277–281 (1992).
36. J. H. Noh, S. H. Im, J. H. Heo, T. N. Mandal, S. I. Seok, Chemical management for colorful, efficient, and stable inorganic–organic hybrid nanostructured solar cells. *Nano Lett.* **13**, 1764–1769 (2013).
37. N. Arora, M. I. Dar, M. Hezam, W. Tress, G. Jacopin, T. Moehl, P. Gao, A. S. Aldwayyan, B. Deveaud, M. Grätzel, M. K. Nazeeruddin, Photovoltaic and amplified spontaneous emission studies of high-quality formamidinium lead bromide perovskite films. *Adv. Funct. Mater.* **26**, 2846–2854 (2016).
38. T. Chen, B. J. Foley, B. Ipek, M. Tyagi, J. R. D. Copley, C. M. Brown, J. J. Choi, S.-H. Lee, Rotational dynamics of organic cations in the $CH_3NH_3PbI_3$ perovskite. *Phys. Chem. Chem. Phys.* **17**, 31278–31286 (2015).
39. A. Mattoni, A. Filippetti, M. I. Saba, P. Delugas, Methylammonium rotational dynamics in lead halide perovskite by classical molecular dynamics: The role of temperature. *J. Phys. Chem. C* **119**, 17421–17428 (2015).
40. S. Meloni, T. Moehl, W. Tress, M. Franckevičius, M. Saliba, Y. H. Lee, P. Gao, M. K. Nazeeruddin, S. M. Zakeeruddin, U. Rothlisberger, M. Graetzel, Ionic polarization-induced current–voltage hysteresis in $CH_3NH_3PbX_3$ perovskite solar cells. *Nat. Commun.* **7**, 10334 (2016).
41. A. Filippetti, P. Delugas, M. I. Saba, A. Mattoni, Entropy-suppressed ferroelectricity in hybrid lead-iodide perovskites. *J. Phys. Chem. Lett.* **6**, 4909–4915 (2015).
42. H. Friedrich, *Theoretical Atomic Physics* (Springer, 1990).
43. J. Even, L. Pedesseau, C. Katan, Analysis of multivalley and multibandgap absorption and enhancement of free carriers related to exciton screening in hybrid perovskites. *J. Phys. Chem. C* **118**, 11566–11572 (2014).
44. S. Meloni, G. Palermo, N. Ashari-Astani, M. Gratzel, U. Rothlisberger, Valence and conduction band tuning in halide perovskites for solar cell applications. *J. Mater. Chem. A*, 10.1039/C6TA04949D (2016).
45. A. M. A. Leguy, J. M. Frost, A. P. McMahon, V. G. Sakai, W. Kockelmann, C. Law, X. Li, F. Foglia, A. Walsh, B. C. O'Regan, J. Nelson, J. T. Cabral, P. R. F. Barnes, The dynamics of methylammonium ions in hybrid organic–inorganic perovskite solar cells. *Nat. Commun.* **6**, 7124 (2015).
46. C. Wehrenfennig, M. Liu, H. J. Snaith, M. B. Johnston, L. M. Herz, Charge carrier recombination channels in the low-temperature phase of organic-inorganic lead halide perovskite thin films. *APL Mater.* **2**, 081513 (2014).
47. F. Panzer, S. Baderschneider, T. P. Gujar, T. Unger, S. Bagnich, M. Jakoby, H. Bässler, S. Hüttner, J. Köhler, R. Moos, M. Thelakkat, R. Hildner, A. Köhler, Reversible laser induced amplified spontaneous emission from coexisting tetragonal and orthorhombic phases in hybrid lead halide perovskites. *Adv. Opt. Mater.* **4**, 917–928 (2016).
48. J. M. Frost, K. T. Butler, F. Brivio, C. H. Hendon, M. van Schilfgaarde, A. Walsh, Atomistic origins of high-performance in hybrid halide perovskite solar cells. *Nano Lett.* **14**, 2584–2590 (2014).
49. I. T. Todorov, W. Smith, K. Trachenko, M. T. Dove, DL_POLY_3: New dimensions in molecular dynamics simulations via massive parallelism. *J. Mater. Chem.* **16**, 1911–1918 (2006).
50. J. P. Perdew, K. Burke, M. Ernzerhof, Generalized gradient approximation made simple. *Phys. Rev. Lett.* **77**, 3865–3868 (1996).
51. A. M. Rappe, K. M. Rabe, E. Kaxiras, J. D. Joannopoulos, Optimized pseudopotentials. *Phys. Rev. B* **41**, 1227–1230 (1990).
52. H. J. Monkhorst, J. D. Pack, Special points for Brillouin-zone integrations. *Phys. Rev. B* **13**, 5188–5192 (1976).
53. P. Giannozzi, S. Baroni, N. Bonini, M. Calandra, R. Car, C. Cavazzoni, D. Ceresoli, G. L. Chiarotti, M. Cococcioni, I. Dabo, A. Dal Corso, S. de Gironcoli, S. Fabris, G. Fratesi, R. Gebauer, U. Gerstmann, C. Gougoussis, A. Kokalj, M. Lazzeri, L. Martin-Samos, N. Marzari, F. Mauri, R. Mazzarello, S. Paolini, A. Pasquarello, L. Paulatto, C. Sbraccia, S. Scandolo, G. Sclauzero, A. P. Seitsonen, A. Smogunov, P. Umari, R. M. Wentzcovitch, QUANTUM ESPRESSO: A modular and open-source software project for quantum simulations of materials. *J. Phys. Condens. Matter* **21**, 395502 (2009).
54. C. C. Stoumpos, C. D. Malliakas, M. G. Kanatzidis, Semiconducting tin and lead iodide perovskites with organic cations: Phase transitions, high mobilities, and near-infrared photoluminescent properties. *Inorg. Chem.* **52**, 9019–9038 (2013).

Acknowledgments

Funding: M.I.D., S.M.Z., and M.G. thank the King Abdulaziz City for Science and Technology and the Swiss National Science Foundation (SNSF) for financial support. G.J. acknowledges financial support from the SNSF under project no. 154853. U.R. acknowledges funding from the SNSF through individual grant no. 200020-146645 and the National Centres of Competence in Research projects MUST and MARVEL and the NRP70. A.M. acknowledges funding from the Italian Ministry of Higher Education through the MIUR-PON Netergit grant. This work was supported by a grant from the Swiss National Supercomputing Centre under project ID s426 and by CINECA, Italy, through the Italian SuperComputing Resource Allocation project VIPER. **Author contributions:** M.I.D. and G.J. designed and performed PL measurements. M.I.D., G.J., and S.M. analyzed and interpreted the PL data. S.M., A.M., and U.R. conceived the computational studies. A.M. carried out MD simulations, and S.M. performed first-principle simulations with the assistance of A.B. N.A. and M.I.D. prepared and structurally and morphologically characterized the perovskite films. M.I.D. wrote the manuscript, together with G.J. and S.M., and U.R. made some contributions to the manuscript writing. All the authors contributed to finalizing the draft. S.M.Z. coordinated the research, and U.R. and M.G. supervised the project. **Competing interests:** The authors declare that they have no competing interests. **Data and materials availability:** All data needed to evaluate the conclusions in the paper are present in the paper and/or the Supplementary Materials. Additional data related to this paper may be requested from the authors.

Submitted 21 May 2016
Accepted 27 September 2016
Published 28 October 2016
10.1126/sciadv.1601156

Citation: M. I. Dar, G. Jacopin, S. Meloni, A. Mattoni, N. Arora, A. Boziki, S. M. Zakeeruddin, U. Rothlisberger, M. Grätzel, Origin of unusual bandgap shift and dual emission in organic-inorganic lead halide perovskites. *Sci. Adv.* **2**, e1601156 (2016).

Science Advances

Origin of unusual bandgap shift and dual emission in organic-inorganic lead halide perovskites

M. Ibrahim Dar, Gwénolé Jacopin, Simone Meloni, Alessandro Mattoni, Neha Arora, Ariadni Boziki, Shaik Mohammed Zakeeruddin, Ursula Rothlisberger and Michael Grätzel

Sci Adv **2** (10), e1601156.
DOI: 10.1126/sciadv.1601156